Optomechanical transduction of an integrated silicon cantilever probe using a microdisk resonator

Kartik Srinivasan,*,† Houxun Miao,†,‡ Matthew T. Rakher,† Marcelo Davanço,†,‡ and Vladimir Aksyuk*,†,¶

Center for Nanoscale Science and Technology, National Institute of Standards and Technology, Gaithersburg, MD 20899, USA

E-mail: kartik.srinivasan@nist.gov; vladimir.aksyuk@nist.gov

Abstract

Sensitive transduction of the motion of a microscale cantilever is central to many applications in mass, force, magnetic resonance, and displacement sensing. Reducing cantilever size to nanoscale dimensions can improve the bandwidth and sensitivity of techniques like atomic force microscopy, but current optical transduction methods suffer when the cantilever is small compared to the achievable spot size. Here, we demonstrate sensitive optical transduction in a monolithic cavity-optomechanical system in which a sub-picogram silicon cantilever with a sharp probe tip is separated from a microdisk optical resonator by a nanoscale gap. High quality factor ($Q \approx 10^5$) microdisk optical modes transduce the cantilever's MHz frequency thermally-driven vibrations with a displacement sensitivity of $\approx 4.4 \times 10^{-16}$ m/$\sqrt{\text{Hz}}$ and bandwidth > 1 GHz, and a dynamic range $> 10^6$ is estimated for a 1 s measurement. Optically-induced stiffening due to the strong optomechanical interaction is observed, and engineering of probe dynamics through cantilever design and electrostatic actuation is illustrated.

*To whom correspondence should be addressed

†Center for Nanoscale Science and Technology, National Institute of Standards and Technology, Gaithersburg, MD 20899, USA

‡Maryland Nanocenter, University of Maryland, College Park, MD 20742

¶Department of Electrical and Computer Engineering, University of Maryland, College Park, MD 20742

Keywords: Cavity optomechanics, atomic force microscopy, nanomechanics, motion detection, nanophotonics

Micro- and nanoscale cantilevers are at the heart of many applications in mass, force, magnetic resonance, and displacement sensing.[1–4] In atomic force microscopy (AFM),[5] the push towards smaller cantilevers[6,7] is motivated by the ability to increase mechanical frequencies while maintaining a desired level of stiffness. This influences the force sensitivity and measurement bandwidth, in turn determining the image acquisition rate and ability to resolve time-dependent forces and acquire additional information about the tip-sample interaction potential.[8] Standard optical methods for transducing cantilever motion include beam deflection[9] and laser interferometry,[10] and in macroscopic devices that are 1 mm $\times$ 1 mm $\times$ 60 μm (length, width, and height), quantum-limited displacement sensitivity of 4×10^{-19} m/$\sqrt{\text{Hz}}$ has been achieved.[11] Interferometric approaches using a high numerical aperture objective have also been used in micro-scale devices, resulting in displacement sensitivities of 3×10^{-14} m/$\sqrt{\text{Hz}}$ for cantilevers that are 20 μm $\times$ 4 μm$\times$ 0.2 μm and 1×10^{-15} m/$\sqrt{\text{Hz}}$ for larger conventional cantilevers (223 μm $\times$ 31 μm$\times$ 6.7 μm).[12] However, as the cantilever dimensions are pushed below the detection wavelength, diffraction effects limit the sensitivity of these approaches,[13] and near-field optics and/or integrated on-chip detection methods can be of significant benefit.

To that end, researchers have recently used evanescently coupled on-chip waveguides[14] acting as doubly-clamped cantilevers[15,16] to demonstrate displacement sensitivities of 3.5×10^{-14} m/$\sqrt{\text{Hz}}$, while end-to-end waveguides acting as singly-clamped devices[17] have achieved similar performance.[18] Although these waveguide-based approaches are optically broadband, the strong, multi-pass interaction provided by optical cavities can be of considerable advantage. Cavity optomechanics[19–21] has seen substantial recent progress, where in many cases the optical resonator also acts as a mechanical oscillator, and its internal vibrations have been transduced with measurement imprecision at or below the standard quantum limit[22,23] and with absolute displacement sensitivities in the 10^{-17} m/$\sqrt{\text{Hz}}$ to 10^{-18} m/$\sqrt{\text{Hz}}$ range.[24,25] In contrast, here we focus on transducing the motion of a cantilever probe, requiring a design in which the cantilever can be brought near a surface and its fluctuations sensed by a nearby optical cavity without inducing excessive optical loss.

A similar approach was presented in Ref.,[26] where doubly-clamped SiN_x nanobeams were brought into the near-field of SiO_2 microtoroid cavities fabricated on a separate chip. In comparison, here we fabricate a cantilever-optical cavity system on a single silicon device layer, while tailoring the cantilever geometry for both strong optomechanical interactions and applicability to AFM. Beyond demonstrating sub-fm/$\sqrt{\mathrm{Hz}}$ sensitivity to cantilever motion, this approach has many potential benefits for AFM. Silicon's high refractive index allows for significantly smaller optical cavities to be used, yielding stronger cantilever-cavity coupling rates and permitting higher bandwidth operation. Moving to silicon opens up potentially advanced device functionality, including electrostatic actuation and integrated optical waveguide readout. By largely separating the mechanical and optical designs, engineering of the cantilever geometry to achieve desired parameters can be accomplished without adversely affecting the optical readout mechanism. In addition, the strong optomechanical interaction can allow for optical control of cantilever mechanics, through effects such as optically-induced stiffening and optically-driven mechanical vibrations.[19,20,24,27] Finally, this platform provides simplifications with respect to free-space detection systems that may improve measurement stability and be of importance in parallelized multi-probe measurements[28] or environments with limited optical access. In particular, the monolithic integration of cantilever and optical sensor on a single chip suppresses unwanted differential motion between the two elements that may be caused by vibrations in the experimental setup. This work lays the foundations for a class of practical nanoscale mechanical sensors enabled by cavity optomechanics.

Device geometry and simulation

A simple device geometry is shown in 1(a), with fabrication details given in the Supporting Information. A semicircular cantilever of width W is suspended at its ends and separated by a gap G from a 10 μm diameter silicon microdisk. The silicon is 260 nm thick, and the cantilever has been designed to support a sharp tip at its midpoint. Devices are fabricated with W=65 nm, 100 nm, and 200 nm, and nominal values G=50 nm, 75 nm, and 100 nm. Scanning electron microscope

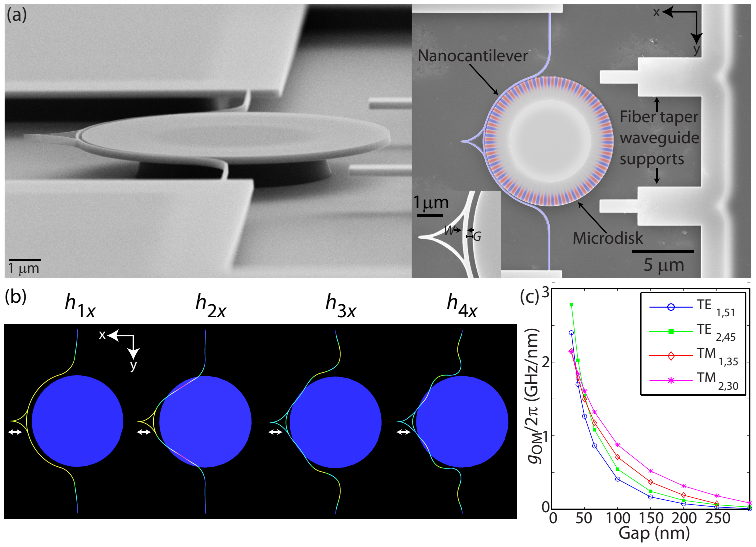

Figure 1: (a) Scanning electron micrographs of the cantilever-microdisk system. The right image has the FEM-calculated z-component of the magnetic field for the $TE_{1,51}$ mode overlaid on the structure, while the inset shows a zoomed-in region with cantilever width W and gap G; (b) Simulated mechanical modes (amplitude exaggerated for clarity) with dominant displacement along the x-axis for W=65 nm; (c) Predicted optomechanical coupling g_{OM} between the h_{1x} cantilever mode and TE/TM modes of the microdisk.

(SEM) images indicate that W is typically within $\pm$5 nm of its nominal value, while G is often smaller than the nominal value by a couple tens of nanometers, though charging effects due to the electron beam limit this estimate. The cantilever geometry is chosen to maximize its interaction with microdisk optical modes while minimizing the scattering loss induced by its presence. In particular, the cantilever is curved around the microdisk so that it interacts with it over almost half the microdisk circumference, while the cantilever smoothly transitions into and out of the disk near-field to avoid abrupt transitions and limit scattering loss. Optical modes are labeled $TE_{p,n}$ and $TM_{p,n}$, according to polarization (transverse electric or transverse magnetic) and radial (p) and azimuthal (n) order. Three-dimensional finite element method (FEM) eigenfrequency simulations indicate that, for W=65 nm or W=100 nm, cavity quality factors (Qs) in excess of 10^6 can be achieved for $TE_{1,n}$ and $TE_{2,n}$ modes, and Qs in excess of 10^5 can be achieved for $TM_{1,n}$ modes, even as G decreases to $\approx$30 nm. In comparison and as a baseline, fabricated microdisks without cantilevers exhibit Qs in the mid-10^5 to low-10^6 range.

Mechanical modes of a W=65 nm cantilever are determined from FEM simulations (see Supporting Information), with representative modes shown in 1(b). We have focused on the h_{mx} modes, which are even symmetry in-plane modes whose primary displacement direction is normal to the gap (x direction), as they are the dominant modes that are optically transduced and are of particular relevance to AFM work. The predicted stiffness (k), resonant frequency (Ω_M), and effective mass (m) of these modes are compiled in 1. Focusing on the h_{1x} mode at $\Omega_M/2\pi = 2.23$ MHz, its optomechanical coupling to p=1 and p=2 optical modes in the 1550 nm band, defined as $g_{\mathrm{OM}} = d\omega_c/dG$ (ω_c is the cavity mode frequency), is calculated by FEM simulation and displayed in 1(c). For the range of gaps studied in this work, $g_{\mathrm{OM}}/2\pi \approx 0.5$ GHz/nm to $g_{\mathrm{OM}}/2\pi \approx 3.0$ GHz/nm. This is about two orders of magnitude larger than g_{OM} for SiN_x cantilevers coupled to SiO_2 microtoroids,[26] and is due to the more tightly confined optical modes supported by the silicon microdisks.

Table 1: Calculated and measured properties of the h_{mx} cantilever modes.

Mode	k (calc.)	m (calc.)	$\Omega_M/2\pi$ (calc.)	$\Omega_M/2\pi$ (expt.)	$\Gamma_M/2\pi$ (expt.)	Q_M (expt.)
h_{1x}	0.14 N/m	0.73 pg	2.23 MHz	2.35 MHz	479 ± 8 kHz	4.9
h_{2x}	1.41 N/m	0.58 pg	7.82 MHz	7.89 MHz	598 ± 11 kHz	13.1
h_{3x}	5.72 N/m	0.35 pg	20.37 MHz	20.51 MHz	533 ± 2 kHz	38.5
h_{4x}	12.43 N/m	0.32 pg	31.17 MHz	31.36 MHz	706 ± 4 kHz	44.4
h_{5x}	41.95 N/m	0.44 pg	49.36 MHz	49.86 MHz	815 ± 4 kHz	61.2
h_{6x}	74.05 N/m	0.40 pg	68.13 MHz	68.71 MHz	752 ± 43 kHz	91.0

Transduction of cantilever motion

We measure the fabricated devices using a fiber taper coupling method[29,30] shown schematically in 2(a) (see Supporting Information). A 1550 nm band tunable diode laser is attenuated and coupled into the devices using an optical fiber taper waveguide (FTW). The FTW is a single mode optical fiber whose minimum diameter has been adiabatically and symmetrically reduced to a wavelength-scale diameter of about 1 μm with low loss (FTW transmission > 50 %). At this diameter, the FTW optical mode spatial profile extends well beyond the glass core into the surrounding air cladding. The evanescent tail of this propagating waveguide mode has a large enough spatial overlap with the modes of interest of the microdisk cavity (the $TE_{1,n}$, $TE_{2,n}$ modes, and $TM_{1,n}$ modes) to efficiently couple into and out of them, with critical coupling (complete power transfer) achievable. The signal exiting the cavity is split by a 90:10 fiber coupler, with 10 % of the light used for monitoring the transmission level and recording swept-wavelength transmission spectra, and 90 % sent into a radio frequency (RF) photodetector, after which an electronic spectrum analyzer measures RF oscillations in the detected signal.

Normalized transmission spectra over the full wavelength band for TE and TM polarized modes of a $W = 65$ nm, $G = 50$ nm device are shown in 2(b), along with zoomed-in scans of individual modes. The polarization of the modes is determined by comparing the free spectral ranges for modes of a given radial order with those predicted from simulation. Loaded cavity Qs of 8.0×10^4 and 1.8×10^5 are observed for this device (corresponding intrinsic Qs of 1.1×10^5 and 2.1×10^5, respectively), which supports doublet modes due to surface-roughness-induced backscattering that couples the clockwise and counterclockwise modes of the cavity.[31] Over all devices, Qs of 5×10^4 to 2×10^5 are typically observed for $TE_{1,n}$, $TE_{2,n}$ and $TM_{1,n}$ modes, though occasional devices have Qs as high as $\approx 6\times10^5$ (see supplemental data). Optical transduction of the cantilever's motion due to thermal noise is performed by fixing the laser on the blue-detuned shoulder of a TE-polarized cavity mode. A 1 MHz to 600 MHz spectrum for a $W = 65$ nm, $G = 100$ nm device is shown in 2(c), and contains several peaks. Those below 100 MHz originate from motion of the cantilever, while those at higher frequencies (364.63 ± 0.35 MHz and 577.20 ± 0.25 MHz) are from motion of the disk. This is confirmed by measuring the RF spectrum of a disk without a cantilever (2(d)) through a high-Q cavity mode (loaded $Q = 5.7\times10^5\pm0.5\times10^5$, intrinsic $Q \approx 1.0\times10^6$), which yields RF peaks at near-identical frequencies (364.74 ± 0.03 MHz and 576.20 ± 0.03 MHz). FEM simulations indicate that the higher frequency mode is the disk's radial breathing mode (*RBM*); its measured linewidth is $\Gamma_M/2\pi = 21.68\pm0.06$ MHz, corresponding to $Q_M \approx 27$.

Focusing on the frequency range between 100 kHz and 100 MHz, a higher resolution RF spectrum at 223 μW of input power (P_{in}) into the cavity is shown in 2(e). The frequencies of the transduced modes (1) correspond well with the previously described simulation results. The mechanical quality factors of these modes are between $Q_M \approx 5$ for the h_{1x} mode and $Q_M \approx 61$ for the h_{5x} mode (1); these values are likely limited by air damping.[32] The detection background, shown in

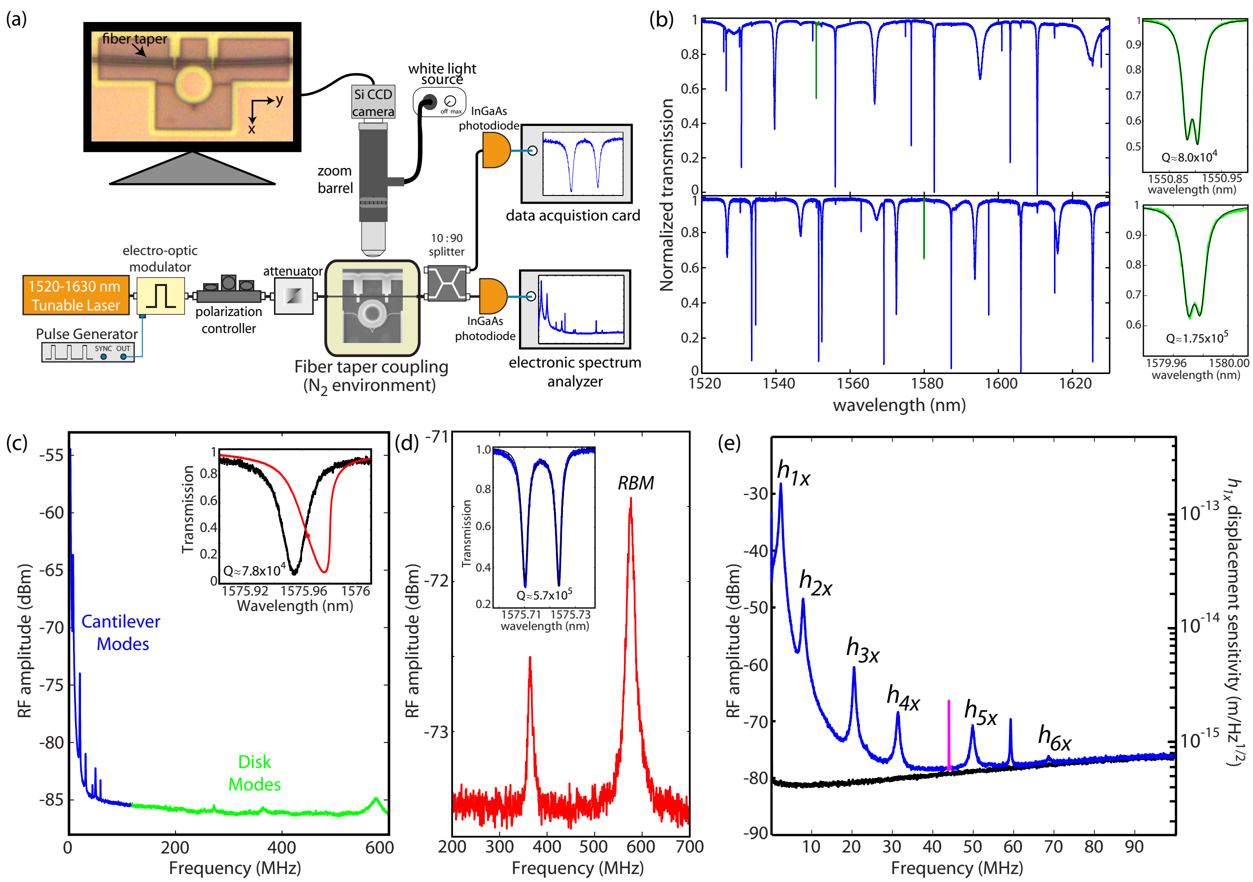

Figure 2: (a) Setup for device characterization. (b) Broad wavelength scan (left) for TE (top) and TM (bottom) modes of a typical disk-cantilever device (W=65 nm, G=50 nm). Zoomed-in scans (right) show data (green) along with a doublet model fit (black). (c) Broad RF spectrum of a disk-cantilever device (W=65 nm, G=100 nm), transduced by fixing the probe laser on the short wavelength side of the TE-polarized mode shown in the inset (black=low power, $P_{\text{in}} = 14.1\mu\, W$, red=high power, $P_{\text{in}} = 223\mu\, W$). Mechanical modes below 100 MHz (blue) are due to the cantilever, while modes at 364.63 MHz and 577.20 MHz (green) are due to the disk. (d) RF spectrum of a disk *without* the cantilever, displaying modes at 364.74 MHz and 576.20 MHz. The inset shows a high-Q TE optical mode of the disk (blue) with fit (black). (e) Zoomed-in RF spectrum of the disk-cantilever, showing the h_{mx} modes (blue), calibration peak (purple), and detection background (black).

2(e) in black, is found by placing the laser off-resonance while maintaining a fixed detected power. Focusing on the h_{1x} mode, its calculated effective mass and measured frequency correspond to a peak displacement amplitude of $x_{rms} = \sqrt{k_B T/k} \approx 160$ pm when driven by thermal noise at 300 K. We use x_{rms} and Γ_M to convert the RF amplitude in 2(e) to displacement sensitivity.[1] The corresponding photodetector-limited sensitivity is $4.4\times10^{-16}\pm0.3\times10^{-16}$ m/$\sqrt{\text{Hz}}$. This value is consistent with that determined by a phase modulator calibration (Supporting Information) to within our uncertainty in the disk-cantilever gap. It represents an improvement by about a factor of 100 with respect to other on-chip silicon cantilever experiments,[15,18] is at the same absolutely sensitivity level demonstrated for SiN_x cantilevers transduced by silica microtoroids,[26] and is about a factor of 5 times larger than the standard quantum limit[33] for our system. Along with the sensitivity, two other important quantities that characterize this system for its use as a displacement sensor are its dynamic range and bandwidth. The maximum detectable displacement is approximately the ratio of the cavity linewidth ($\Gamma/2\pi = 2.44$ GHz) to g_{OM}, and is ≈ 4 nm, giving a dynamic range $> 10^6$ (60 dB) for a 1s measurement. The bandwidth (BW) is limited by the cavity's response time, which determines how quickly it can transduce mechanical motion. We therefore expect a BW$>$ 1 GHz, and this is substantiated by transduction of the 575 MHz oscillations of the disk as previously described in 2(c)-(d). Adjusting the BW (e.g., through the waveguide coupling) allows for gain/BW tradeoff within the fixed gain-BW product. The large BW of these devices is one advantage of relying on large g_{OM} rather than ultra-high-Q for displacement detection.

Optically-induced stiffening

Increasing the optical power coupled into the cavity causes several notable changes in the RF spectrum, as seen in 3(a)-(b) for a W=65 nm, $G = 75$ nm device, where the coupled power is changed by fixing $P_{\text{in}} = 446$ μW and varying the detuning $\Delta\lambda$ between the laser and cavity mode. First, the spectral position of the h_{1x} mode changes from $\Omega_M/2\pi \approx 2.24$ MHz at large $\Delta\lambda$ to $\Omega'_M/2\pi \approx 3.26$ MHz at $\Delta\lambda = -21$ pm before returning to close to its original value at near-zero $\Delta\lambda$ (3(c)). One explanation for this is the optical spring effect, an optically-generated rigidity of the mechanical oscillator, as seen in other works.[19,24,27,34] In particular, if we take the

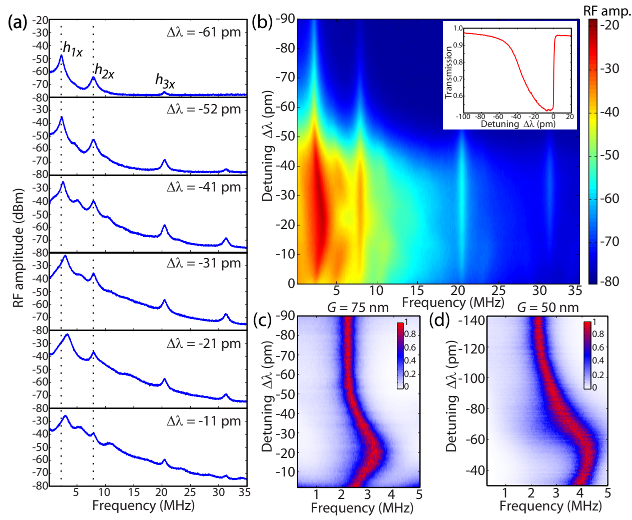

Figure 3: (a) RF spectra from a device (W=65 nm, G=75 nm) with $P_{in} = 446\ \mu$W at different laser-cavity detunings $\Delta\lambda$. (b) Image plot of the RF spectra as a function of $\Delta\lambda$. The cavity mode used for transduction is shown in the inset. (c) Zoomed-in portion of the image plot for the h_{1x} mode, showing optically-induced stiffening. (d) Zoomed-in image plot for the h_{1x} mode of a W=65 nm, G=50 nm device. In (c)-(d), the RF spectra are displayed on a linear scale, with each spectrum normalized to the peak amplitude for that value of $\Delta\lambda$.

measured values for Ω_M, Ω'_M, $\Delta\lambda$, Γ, and internal cavity energy U (determined by P_{in}, transmission contrast, and Γ), the value of g_{OM} that best matches the maximum frequency shift is $g_{\text{OM}}/2\pi = 1.4$ GHz/nm, corresponding to a gap $G \approx 60$ nm for the $\text{TE}_{2,45}$ mode. Similarly, 3(d) shows a shift from $\Omega_M/2\pi \approx 2.26$ MHz at large $\Delta\lambda$ to $\Omega'_M/2\pi \approx 4.25$ MHz at $\Delta\lambda = -41$ pm, in this case for the h_{1x} mode of a W=65 nm, G =50 nm device. This shift is consistent with $g_{\text{OM}}/2\pi = 3.0$ GHz/nm, corresponding to a gap $G \approx 32$ nm for the $\text{TE}_{2,45}$ mode. Both of these gaps are smaller than the nominal values, but are reasonable given the variation observed in SEM images of fabricated devices.

Along with the change in frequency, the linewidth of the h_{1x} mode changes from $\Gamma_M/2\pi \approx 410$ kHz at $\Delta\lambda = -61$ pm to $\Gamma_M/2\pi \approx 860$ kHz at $\Delta\lambda = -21$ pm, indicating damping. In addition, the increase in RF amplitude of the h_{mx} modes is accompanied by a broad background which, in certain detuning ranges, produces peaks in the RF spectrum not seen at lower powers and at frequencies that are not predicted by mechanical simulations of the cantilever. The precise nature of these effects is not understood, though a likely cause is the interplay between free-carrier and thermal

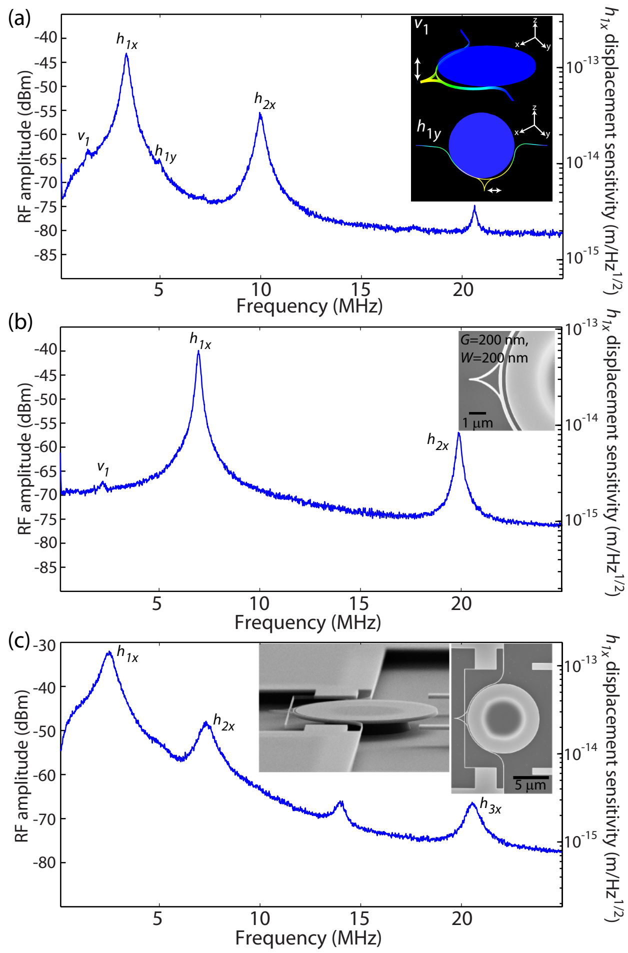

Figure 4: (a) RF spectrum from a disk-cantilever with W=100 nm, G=200 nm. Inset shows displacement profiles for cantilever modes not shown in 1(b). (b) RF spectrum from a device with W=200 nm, G=200 nm. (c) RF spectrum from a disk-double-cantilever with W=65 nm, G=50 nm. Inset shows SEMs of the device geometry.

effects that takes place in silicon microdisks as the intracavity energy is increased. Measurements of devices with and without cantilevers (supporting information) show behavior consistent with previous observation of such effects.[35] It should also be noted that thermal effects have been observed to generate damping for blue-detuned excitation in other optomechanical systems.[24]

Cantilever engineering and outlook

While optically-induced stiffening provides real-time control of the cantilever properties over a certain range, a number of modifications to its geometry can improve its applicability to different AFM applications. The sub-N/m spring constant of the h_{1x} mode is suitable for weak force measurements in which the cantilever is undriven, but in dynamic techniques for which the best imaging conditions have been achieved, such as frequency modulation AFM,[36] spring constants in the tens of N/m to hundreds of N/m range (or more) are desirable for small amplitude operation.[5] In our geometry, the cantilever stiffness may be increased by increasing its width; figs. 4(a)-(b) show the mechanical mode spectra for W=100 nm and W=200 nm devices. The h_{1x} modes at $\Omega_M/2\pi = 3.33$ MHz and $\Omega_M/2\pi = 6.96$ MHz agree well with the simulated values of 3.42 MHz and 7.22 MHz. Based on the calculated effective masses, these values correspond to a cantilever stiffness of 0.52 N/m and 4.11 N/m, respectively, with the latter being a 30$\times$ increase in stiffness relative to the h_{1x} mode of the $W = 65$ nm device. Stiffer cantilevers can be produced by a further increase in W, though degradation in the optical Q is expected unless G is increased, which can then limit the displacement sensitivity due to a reduced g_{OM}. Another option is to reduce the cantilever length between its suspension points. To maintain a strong optomechanical coupling, this can be done by simultaneously reducing the disk diameter so that the cantilever continues to interact with the disk over nearly half its circumference. Bare microdisks have radiation-limited Qs $> 10^6$ until their diameters are just a couple of micrometers,[37] and simulations predict that the h_{1x} mode of a W=100 nm cantilever coupled to a 4.5 μm diameter disk will occur at 7.96 MHz ($k = 1.8$ N/m). Another important consideration is the modal structure of the cantilever. Though we have focused on the h_{1x} mode due to its displacement profile and transduction under thermal noise, in an AFM setting, the cantilever motion will be defined by both its actuation mechanism and the surface it is interrogating, and its motion will be a superposition of its modes. This includes out-of-plane (z direction) and orthogonal in-plane (y direction) modes such as those seen weakly in the RF spectra of 4(a)-(b). Engineering of the cantilever support geometry can better isolate the h_{1x} mode in frequency space. The double cantilever structure shown in the SEM images of 4(c) has h_{1x} as its lowest frequency mode, with the first out-of-plane mode v_1 significantly stiffened and shifted to higher frequencies. Figure 4(c) shows an optically-transduced RF spectrum for such a device, with W=65 nm. Going forward, further modifications may be made to increase the stiffness of the cantilever, for example, through multiple short supports to surrounding areas. By combining this approach with W=200 nm cantilevers and/or smaller diameter disks, we expect that k=100 N/m

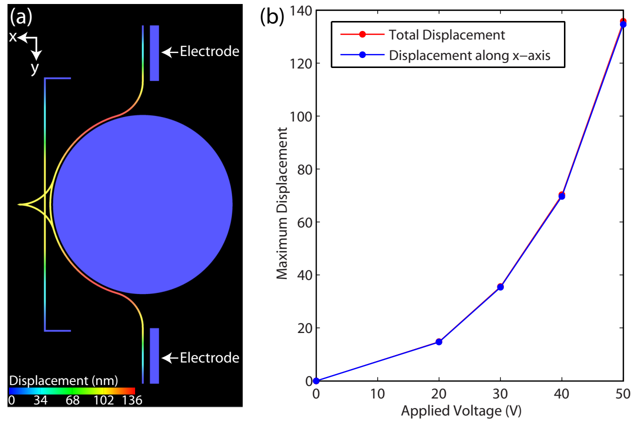

Figure 5: (a) Simulated displacement profile for a disk-double-cantilever under application of 50 V to electrodes placed at the sides of the cantilevers. (b) Calculated maximum overall displacement and displacement along the x-axis as a function of applied voltage.

devices will be achievable. On the opposite end of the spectrum, very soft cantilevers are also of considerable interest, due to their application in measurements of very small forces[38] such as in magnetic resonance force microscopy.[39] Reducing the cantilever spring constant by as much as two orders of magnitude can involve simply increasing the cantilever length and clamping it only on a single side.

Future dynamic AFM measurements will require an actuation mechanism for driving the cantilever's motion. As an illustration of one approach, we consider electrostatic actuation through a pair of fixed electrodes that are placed 350 nm to the side of the double cantilever geometry (5). Finite element modeling shows that stable, steady-state displacements in excess of 100 nm can be achieved with an applied voltage under 50 V. We also note that the displacement is primarily ($>$ 99 %) along the x-axis, confirming the effectiveness of the cantilever mode engineering described above. In practice, applications such as frequency modulation AFM will require much smaller displacements, and regardless, the maximum detectable displacement under the current scheme is ≈ 4 nm. This displacement level should be achievable for an applied voltage near 5 V. We can then estimate the performance of this system in a frequency modulation AFM scheme using the results from Ref.,[36] along with the h_{1x} mode frequency $\Omega_M/2\pi$=2.48 MHz and linewidth $\Gamma_M/2\pi$=603$\pm$4 kHz for the device of 4(c). The minimum detectable force F_{min} and force gradient $\delta F'_{\text{min}}$ are $F_{\text{min}} = \sqrt{(4kk_BTB)/(\Omega_M Q_M)}$=5.1$\times 10^{-14}$ N and $\delta F'_{\text{min}} = \sqrt{(4kk_BTB)/(\Omega_M Q_M A^2)}$=1.2$\times 10^{-5}$ N/m, where

A is the cantilever oscillation amplitude (4 nm), and B is the measurement bandwidth, taken to be 50 Hz for comparison to other experiments.[40] Despite operating in an ambient environment with $Q_{\mathrm{M}} \approx 4$, the estimated F_{min} and $\delta F'_{\mathrm{min}}$ values are competitive with a range of systems operated in an ultra-high-vacuum environment. In particular, silicon cantilevers[5] with k=2 N/m, $\Omega_M/2\pi$=75 kHz, and $Q_M = 1.0\times10^5$ have achieved $F_{\mathrm{min}} = 5.9\times10^{-15}$ N and $\delta F'_{\mathrm{min}} = 3.0\times10^{-7}$ N/m, while quartz tuning forks in the qPlus configuration[41] with k=1800 N/m, $\Omega_M/2\pi$=20 kHz, and $Q_M = 2.5\times10^3$ have achieved $F_{\mathrm{min}} = 2.1\times10^{-12}$ N and $\delta F'_{\mathrm{min}} = 1.1\times10^{-2}$ N/m. More recently,[40] ultra-stiff piezo-electric quartz length-extension resonators with k=5.4×10^5 N/m, $\Omega_M/2\pi$=1 MHz, and $Q_M = 2.5\times10^4$ have achieved $F_{\mathrm{min}} = 1.6\times10^{-12}$ N and $\delta F'_{\mathrm{min}} = 8.3\times10^{-3}$ N/m. The disk-cantilever system demonstrated here operates in an attractive region of parameter space that differs from the above sensors, in combining a MHz oscillation frequency with a 0.1 N/m to 10 N/m stiffness (with stiffer geometries potentially feasible).

In summary, we have demonstrated sensitive transduction of the motion of a nanoscale cantilever using a high quality factor microdisk cavity fabricated on the same device layer. Future work will be aimed at understanding the capabilities of this system in AFM measurements. This will include measurements under vacuum to determine ultimate mechanical Q_Ms of the devices, and to ascertain whether effects such as optical cooling and regenerative oscillations[19] are accessible. Functional devices for AFM will require several additional technical steps that are currently under investigation. First, additional lithography and anisotropic silicon etching will be performed to ensure that the cantilever probe tip is overhanging the edge of the chip, so that it can be brought into close proximity to other surfaces. Next, the optical fiber taper waveguide coupling method, though low loss and flexible, will be replaced with more robust waveguide readout through on-chip silicon waveguides that are permanently pigtailed to single mode optical fibers. For full device integration[42] in a frequency modulation AFM setting, the on-chip optics will be combined with electrostatic (or optical) actuation of the cantilever motion. Finally, rather than continuing to measure cantilever-driven intensity fluctuations in the transmitted signal from the cavity, a phase-sensitive scheme might be used to produce a dispersive error signal that will allow the laser to be locked to the cavity. Such an approach should increase the measurement stability (currently at the tens of minutes level) considerably, and a preliminary implementation of such a measurement setup is presented in the supporting information.

Acknowledgement

We thank Lei Chen of the CNST NanoFab for assistance with silicon etch development.

Supporting Information Available

Details related to the device fabrication, simulation, characterization, phase modulator calibration, Hansch-Couillaud polarization spectroscopy, and self-induced optical modulation and free carrier effects are included in supporting information that is available free of charge via the Internet at http://pubs.acs.org.

References

(1) Ekinci, K. L.; Roukes, M. L. *Review of Scientific Instruments* **2005**, *76*, 061101.

(2) Li, M.; Tang, H. X.; Roukes, M. L. *Nature Nanotechnology* **2007**, *2*, 114–120.

(3) Ilic, B.; Craighead, H. G.; Krylov, S.; Senaratne, W.; Ober, C.; Neuzil, P. *J. Appl. Phys.* **2004**, *95*, 3694–3703.

(4) Rugar, D.; Yannoni, C. S.; Sidles, J. A. *Nature* **1992**, *360*, 563–566.

(5) Giessibl, F. *Reviews of Modern Physics* **2003**, *75*, 949–983.

(6) Walters, D. A.; Cleveland, J. P.; Thomson, N. H.; Hansma, P. K.; Wendman, M. A.; Gurley, G.; Elings, V. *Review of Scientific Instruments* **1996**, *67*, 3583–3590.

(7) Kawakatsu, H.; Kawai, S.; Saya, D.; Nagashio, M.; Kobayashi, D.; Toshiyoshi, H.; Fujita, H. *Review of Scientific Instruments* **2002**, *73*, 2317–2320.

(8) Sahin, O.; Magonov, S.; Su, C.; Quate, C. F.; Solgaard, O. *Nature Nanotechnology* **2007**, *2*, 507–514.

(9) Meyer, G.; Amer, N. M. *Appl. Phys. Lett.* **1988**, *53*, 1045–1047.

(10) Rugar, D.; Mamin, H. J.; Guethner, P. *Appl. Phys. Lett.* **1989**, *55*, 2588–2590.

(11) Arcizet, O.; Cohadon, P.; Briant, T.; Pinard, M.; Heidmann, A.; Mackowski, J.; Michel, C.; Pinard, L.; Français, O.; Rousseau, L. *Phys. Rev. Lett.* **2006**, *97*, 133601.

(12) Hoogenboom, B. W.; Frederix, P. L. T. M.; Yang, J. L.; Martin, S.; Pellmont, Y.; Steinacher, M.; Zäch, S.; Langenbach, E.; Heimbeck, H.; Engel, A.; Hug, H. J. *Appl. Phys. Lett.* **2005**, *86*, 074101.

(13) Kouh, T.; Karabacak, D.; Kim, D. H.; Ekinci, K. L. *Appl. Phys. Lett.* **2005**, *86*, 013106.

(14) Povinelli, M. L.; Lončar, M.; Ibanescu, M.; Smythe, E. J.; Johnson, S. G.; Capasso, F.; Joannopoulos, J. D. *Opt. Lett.* **2005**, *30*, 3042–3044.

(15) Li, M.; Pernice, W. H. P.; Tang, H. X. *Nature Photonics* **2009**, *3*, 464–468.

(16) Roels, J.; de Vlaminck, I.; Lagae, L.; Maes, B.; van Thourhout, D.; Baets, R. *Nature Nanotechnology* **2009**, *4*, 510–513.

(17) Pruessner, M. W.; Siwak, N.; Amarnath, K.; Kanakaraju, S.; Chuang, W.; Ghodssi, R. *Journal of Micromechanics and Microengineering* **2006**, *16*, 832–842.

(18) Li, M.; Pernice, W. H. P.; Tang, H. X. *Nature Nanotechnology* **2009**, *4*, 377–382.

(19) Kippenberg, T. J.; Vahala, K. J. *Opt. Express* **2007**, *15*, 17172–17205.

(20) Favero, I.; Karrai, K. *Nature Photonics* **2009**, *3*, 201–205.

(21) van Thourhout, D.; Roels, J. *Nature Photonics* **2010**, *4*, 211–217.

(22) Schliesser, A.; Arcizet, O.; Rivière, R.; Anetsberger, G.; Kippenberg, T. J. *Nature Physics* **2009**, *5*, 509–514.

(23) Teufel, J. D.; Donner, T.; Castellanos-Beltran, M. A.; Harlow, J. W.; Lehnert, K. W. *Nature Nanotechnology* **2009**, *4*, 820–823.

(24) Eichenfield, M.; Camacho, R.; Chan, J.; Vahala, K. J.; Painter, O. *Nature* **2009**, *459*, 550–555.

(25) Schliesser, A.; Anetsberger, G.; Rivière, R.; Arcizet, O.; Kippenberg, T. J. *New Journal of Physics* **2008**, *10*, 095015.

(26) Anetsberger, G.; Arcizet, O.; Unterreithmeier, Q. P.; Rivière, R.; Schliesser, A.; Weig, E. M.; Kotthaus, J. P.; Kippenberg, T. J. *Nature Physics* **2009**, *5*, 909–914.

(27) Sheard, B. S.; Gray, M. B.; Mow-Lowry, C. M.; McClelland, D. E.; Whitcomb, S. E. *Phys. Rev. A* **2004**, *69*, 051801.

(28) Minne, S. C.; Adams, J. D.; Yaralioglu, G.; Manalis, S. R.; Atalar, A.; Quate, C. F. *Appl. Phys. Lett.* **1998**, *73*, 1742–44.

(29) Srinivasan, K.; Barclay, P. E.; Borselli, M.; Painter, O. *Phys. Rev. B* **2004**, *70*, 081306R.

(30) Michael, C. P.; Yuen, H. B.; Sabnis, V. A.; Johnson, T. J.; Sewell, R.; Smith, R.; Jamora, A.; Clark, A.; Semans, S.; Atanackovic, P. B.; Painter, O. *Opt. Express* **2008**, *16*, 19649–19666.

(31) Borselli, M.; Johnson, T. J.; Painter, O. *Opt. Express* **2005**, *13*, 1515–1530.

(32) Verbridge, S. S.; Ilic, R.; Craighead, H. G.; Parpia, J. M. *Appl. Phys. Lett.* **2008**, *93*, 013101.

(33) Caves, C. M.; Thorne, K. S.; Drever, R. W. P.; Sandberg, V. D.; Zimmermann, M. *Rev. Mod. Phys.* **1980**, *52*, 341–392.

(34) Corbitt, T.; Wipf, C.; Bodiya, T.; Ottaway, D.; Sigg, D.; Smith, N.; Whitcomb, S.; Mavalvala, N. *Phys. Rev. Lett.* **2007**, *99*, 160801.

(35) Johnson, T. J.; Borselli, M.; Painter, O. *Opt. Express* **2006**, *14*, 817–831.

(36) Albrecht, T. R.; Grütter, P.; Horne, D.; Rugar, D. *J. Appl. Phys.* **1991**, *69*, 668–673.

(37) Srinivasan, K.; Borselli, M.; Painter, O.; Stintz, A.; Krishna, S. *Opt. Express* **2006**, *14*, 1094–1105.

(38) Stowe, T. D.; Yasumura, K.; Kenny, T. W.; Botkin, D.; Wago, K.; Rugar, D. *Appl. Phys. Lett.* **1997**, *71*, 288–290.

(39) Rugar, D.; Budakian, R.; Mamin, H. J.; Chui, B. W. *Nature* **2004**, *430*, 329–332.

(40) Torbrügge, S.; Schaff, O.; Rychen, J. *J. Vac. S. Tech. B* **2010**, *28*, C4E12–C4E20.

(41) Giessibl, F. J. *Appl. Phys. Lett.* **1998**, *73*, 3956–3958.

(42) Wu, M. C.; Solgaard, O.; Ford, J. E. *J. Lightwave Tech.* **2006**, *24*, 4433–4454.

Supporting Information for Optomechanical Transduction of an Integrated Silicon Cantilever Probe Using a Microdisk Resonator

Kartik Srinivasan,[1,*] Houxun Miao,[1,2] Matthew T. Rakher,[1] Marcelo Davanço,[1,2] and Vladimir Aksyuk[1,3,†]

[1] *Center for Nanoscale Science and Technology, National Institute of Standards and Technology, Gaithersburg, MD 20899, USA*
[2] *Maryland Nanocenter, University of Maryland, College Park, MD 20742*
[3] *Department of Electrical and Computer Engineering, University of Maryland, College Park, MD 20742*

A. Device Fabrication

Devices were created in a silicon-on-insulator wafer with a 260 nm thick device layer, 1 μm thick buried oxide layer, and specified device layer resistivity of 13.5-22.5 ohm-cm (p-type). Fabrication steps included electron-beam lithography of a 400 nm-thick positive-tone resist, an SF_6/C_4F_8 inductively-coupled plasma reactive ion etch through the silicon device layer, a stabilized H_2SO_4/H_2O_2 etch to remove the remnant resist and other organic materials, an HF wet etch to undercut the devices and release the cantilevers, and a critical point dry to finish the processing. The etch time required to go through the silicon device layer is a function of cantilever-disk gap, with an $\approx 30\%$ increase in etch time required for $G = 50$ nm devices relative to $G = 200$ nm devices.

B. Device Simulation

Mechanical eigenfrequencies and eigenmodes of the cantilever and disk were studied using a commercial finite element software package. Silicon was modeled as an elastic cubic material using three independent elastic constants[1] with (100) orientation, and clamped boundary conditions were assumed at the cantilever ends. Mesh refinement studies indicate that numerical errors are below the uncertainty resulting from imperfect knowledge of the cantilever geometry, which is generally a few percent of the reported values. For the reported mode frequencies Ω_M and effective masses m, zero residual stress was assumed. In a separate numerical study, all cantilever mode frequencies were shown to be approximately independent (within a few percent) of the residual stress for stress values under ± 100 MPa. The mode stiffness was calculated as $k = m\Omega_M^2$.

Electrostatic actuation was modeled by iteratively solving a coupled three-dimensional static-mechanical problem and a three-dimensional electrostatic problem. The former fixes the elastic properties and clamped boundary conditions at the four double-cantilever ends to be the same. The mechanically fixed electrodes are 260 nm thick, 500 nm wide, and 3 μm long, and the gap between them and the cantilever is 350 nm. The same fixed voltage is applied to both electrodes (doped silicon is assumed to be a perfect conductor), while the cantilever is assumed to be at the ground potential. Given the applied voltages and shape of the deformable cantilever and fixed electrodes, the electrostatic force densities on all cantilever surfaces are calculated using a boundary element method. The calculated force densities were then applied as boundary conditions and the mechanical problem was solved to find the new deformed beam shape. The electrostatic and mechanical solvers were iterated until the solution converged to a stable value for each applied voltage. Mesh refinement studies were conducted on the electrostatic surface mesh to ensure numerical accuracy. The microdisk and substrate were assumed to be at ground potential and not included in this model for simplicity. This is justified because the cantilever-electrode gap is much smaller than the distances between the electrodes and either the microdisk or substrate.

Optical eigenfrequencies and eigenmodes of the disk-cantilever system were found numerically using a second commercial finite element software package. The silicon layer was modeled as having an index of refraction n=3.4 surrounded by air (n =1), and both materials were assumed lossless and non-magnetic. The size of the three-dimensional model containing the disk, the cantilever, and the surrounding air was chosen to be large enough to fully contain the modes studied, with scattering boundary conditions on the outside surfaces. Mirror symmetry with respect to a plane normal to the disk plane was used to reduce the model volume by half. A mesh refinement study was conducted to ensure numerical accuracy. g_{OM} for the h_{1x} mechanical mode as a function of the gap G was obtained by linearly translating the cantilever with respect to the disk along the x-axis from the initial cantilever-disk gap G=100 nm. For each value of G between 30 nm and 300 nm the cantilever was further deformed using the calculated h_{1x} mode shape. The modal deformations were 0 and $\pm d$, where d varied from 2 nm for $G = 30$ nm to 10 nm for $G >$100 nm. For each G and deformation the frequencies and Qs for multiple optical modes were calculated by numerically

*Electronic address: kartik.srinivasan@nist.gov
†Electronic address: vladimir.aksyuk@nist.gov

solving the eigenvalue problem. For each optical mode and G the derivative of the frequency with respect to modal deformation was obtained using the slope of a linear fit. In all cases, the gap changes and cantilever deformations were implemented by numerically deforming the same original mesh to obtain the desired cantilever shape and position before solving the optical eigenvalue problem.

C. Device Characterization

Devices were characterized using a swept-wavelength external cavity tunable diode laser with a time-averaged linewidth < 90 MHz and absolute stepped wavelength accuracy of ± 1 pm. The wavelength tuning range and linearity are calibrated using an acetylene reference cell, so that the uncertainty in optical cavity Qs is dominated by fits to the data. Light is coupled into and out of the cavities using an optical fiber taper waveguide in a N_2-purged environment at atmospheric pressure and room temperature. Cavity transmission spectra were recorded using a variable gain InGaAs photoreceiver with a typical bandwidth of 775 kHz, noise equivalent power (NEP) of 1.25 pW/$\sqrt{\text{Hz}}$, and gain of 4.5×10^4 V/W. RF spectra were recorded using either a 0 MHz (DC) to 125 MHz InGaAs photoreceiver (NEP=2.5 pW/$\sqrt{\text{Hz}}$, gain=4×10^4 V/W) or DC to 1.1 GHz InGaAs avalanche photodiode (NEP=1.6 pW/$\sqrt{\text{Hz}}$, gain=1.4×10^4 V/W) whose output was sent into a 9kHz to 3.0 GHz electronic spectrum analyzer with resolution bandwidth typically set at 30 kHz. RF frequencies and linewidths are determined by Lorentzian fits to the data, with uncertainties given by the 95 % confidence intervals of the fit (uncertainties are not written if they are smaller than the number of digits to which the value is quoted). Optical frequencies and linewidths are determined by a least squares fit to the data using a doublet model that takes into account both clockwise and counterclockwise whispering gallery modes and their coupling due to backscattering[2].

D. Phase modulator calibration

As a consistency check on the calibration of displacement sensitivity[3], we use an electro-optic phase modulator (Fig. 2(a) of the main text) of known modulation depth $\delta\phi$ and frequency Ω_{mod} to generate a tone in the RF spectrum, at 44 MHz in Fig. 2(e) of the main text. This modulation peak is equivalent to an effective mechanical oscillation amplitude $x_{mod} = \delta\phi(\omega_{mod}/g_{\mathrm{OM}})$, and can provide a check on x_{rms}, but is limited by the accuracy to which g_{OM} is known. For Fig. 2 of the main text, assuming $G = 100$ nm and that the optical mode used for transduction is the $\mathrm{TE}_{2,45}$ mode, $g_{\mathrm{OM}}/2\pi = 0.61$ GHz/nm produces a value $x \approx 192$ pm that is ≈ 20 % greater than $x_{rms} = 160$ pm. A likely source for the discrepancy is imperfect knowledge of the gap; for example, a 10 nm decrease in it would completely account for the difference between the two values.

E. Optical cavity modes and optomechanical coupling

Finite-element method (FEM) simulations indicate that the p=1 and p=2 modes of TE polarization and p=1 modes of TM polarization have high Qs ($> 10^5$) for sufficiently thin cantilevers. Simulation results for W=65 nm cantilevers are shown in Fig. S1(a). Similar simulations for W=100 nm cantilevers indicate a reduction in Q by as much as a factor of 3, though it nevertheless remains above 10^5. As discussed in the text, while most fabricated devices have cavity Qs in the range of 5×10^4 to 2×10^5, a few exhibit Qs as high as $\approx 6\times10^5$ (Fig. S1(b)). The optically transduced RF spectra in such devices often show a strong amplitude for not only the h_{1x} modes, but also h_{my} and v_n modes. This suggests some amount of asymmetry in the cantilever structure not found in the majority of the devices (such as those studied in the main text).

Generally, the measured optical Qs decrease with decreasing gap and increasing cantilever width. Smaller gaps can also be problematic because the time required to etch through the silicon layer goes up as the gap size is reduced, potentially leading to mask erosion and a roughening of the disk sidewalls. The optomechanical coupling g_{OM}, on the other hand, increases with decreasing gap and increasing cantilever width. The calculated g_{OM} for p=1 modes with a W=100 nm cantilever is shown in Fig. S1(c), and can be ≈ 25 % larger than the values calculated for W=65 nm in Fig. 1(d) in the main text.

F. Hansch-Couillaud polarization spectroscopy

For future experiments (including AFM applications) it will likely be necessary to lock the probe laser to the cavity. This can be done by beating the signal exiting the cavity with a strong local oscillator (LO), thereby measuring phase fluctuations due to cantilever motion and giving access to a dispersive signal needed for locking. A particularly convenient approach, Hansch-Couillaud polarization spectroscopy as described in Ref. 3 and shown schematically in Fig. S2(a), sets the polarization so that only part of the input field couples to the cavity, with the orthogonal polarization serving as the LO. The interference signal is analyzed using a $\lambda/4$ waveplate and polarizing beam splitter, whose outputs are measured on a 100 MHz balanced photodetector.

The difference signal produced by scanning the laser over a cavity resonance is shown in the inset to Fig. S2(b). Positioning the laser on resonance and measuring the RF fluctuations in this signal produces the thermal noise spectrum shown in Fig. S2(b).

G. Self-induced optical modulation and free carrier effects

Two-photon absorption is well-known to play an important role in silicon nanophotonics[5], with the subsequent generation of phonons and free carriers giving rise to both optical dispersion and loss, and with the associated lifetimes affecting the speed of devices intended to exploit these effects. In Ref. 6, Johnson *et al.* observed that under sufficiently strong continuous wave input, silicon microdisks of similar dimensions to those studied in this work exhibited steady-state oscillations in their transmitted power. The authors attributed this to competing thermal and free-carrier effects, as the dispersion in the refractive index caused by the two effects is opposite in sign (red-shift for thermal, blue-shift for free carriers), and as the cavity mode position shifts due to this change in refractive index, the circulating power in the cavity changes, thereby changing the rate at which heat and free carriers are created. Looking in the frequency domain, the RF spectrum of the transmitted signal displayed a number of sharp peaks with a spacing of a few hundred kHz. We have observed similar phenomena in our bare (no cantilever) microdisks. Fig. S3(a) shows both a broad (up to 200 MHz) and zoomed-in (up to 15 MHz) spectrum of the transmitted signal from a microdisk with a $Q \approx 3\times10^5$ mode coupled to by a fiber taper waveguide with $P_{\text{in}} \approx 440\ \mu$W at 1533.6 nm. A comb of sharp peaks is observed in the RF spectrum, with a nearest-neighbor spacing that is typically ≈ 3.23 MHz.

The devices shown in the main body of the text have somewhat lower optical Qs than the above device, which likely explains why similarly sharp RF peaks are not observed at similar input powers. Instead, the RF spectra (Fig. 3(a) from the main text)

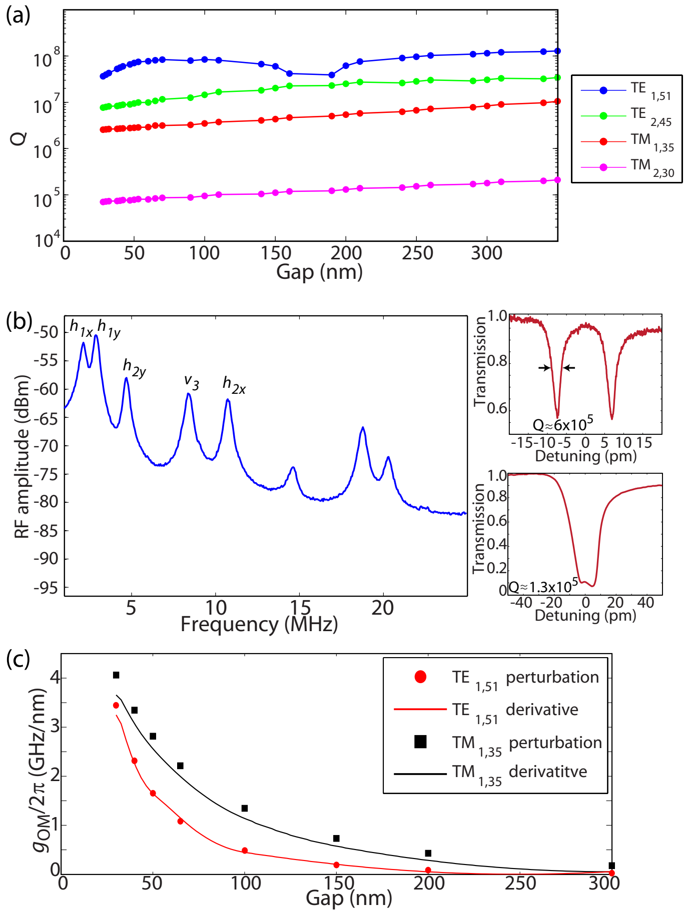

FIG. S1: (a) FEM-calculated optical Qs for TE and TM polarized modes of a disk-cantilever with W=65 nm. (b) Thermal noise spectrum of a G=100 nm, W=100 nm disk-cantilever device. To the right are two optical modes of the structure; the bottom scan is of the mode used in transduction. (c) Predicted optomechanical coupling g_{OM} between the h_{1x} cantilever mode and 1st order radial TE and TM modes of the microdisk. Points are calculated using the perturbation theory method described in Ref. 4, while solid lines are derived from the interpolation of a series of simulations for varying G.

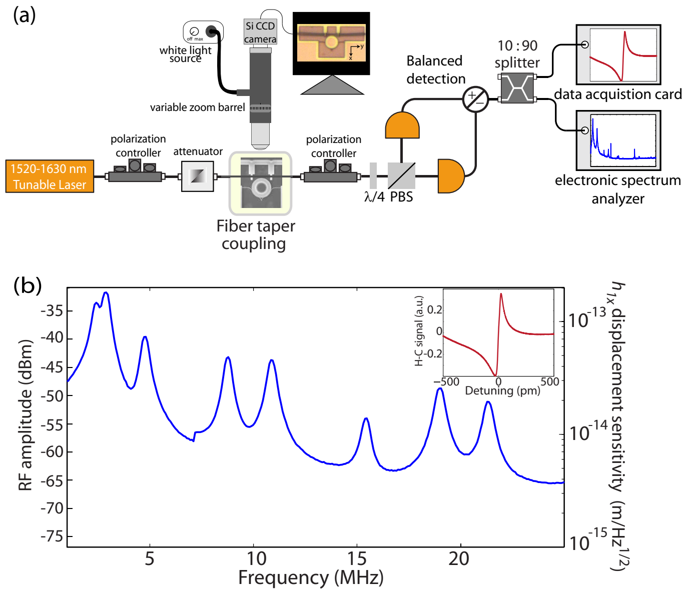

FIG. S2: (a) Schematic of the setup used for Hansch-Couillaud homodyne spectroscopy. The input polarization into the cavity is set so that a small fraction of the signal is coupled into the mode of interest, while the remainder acts as a local oscillator. (b) RF spectrum measured using Hansch-Couillaud homodyne spectroscopy. Inset shows the difference signal produced when the laser is scanned over the cavity resonance.

look to be a superposition of the spectrum due to mechanical oscillations of the cantilever and/or disk and the spectrum due to competing free carrier and thermal effects within the disk, albeit below the threshold for oscillation. To consider this point further, we look at the disk-cantilever device of Fig. S1(b), coupling to a $\mathrm{TE}_{2,n}$ mode with $Q \approx 1.3\times10^5$ (bottom inset of Fig. S1(b)). If we initially restrict $P_{\mathrm{in}} \approx 60$ μW and vary the laser-cavity detuning $\Delta\lambda$, we generate Fig. S3(b). We see that for initial large detunings ($\Delta\lambda = -35$ pm), the RF spectrum is dominated by the mechanical modes of the cantilever, but as the detuning decreases, a background with broad resonances is superimposed ($\Delta\lambda = -31$ pm) and dominates ($\Delta\lambda = -23$ pm), before eventually the mechanical modes re-appear for small enough detunings ($\Delta\lambda = -15$ pm). It is believed that the broad background is due to the same thermal/free-carrier effects seen in Ref. 6 and in the bare disk of Fig. S3(a). Indeed, if P_{in} is increased to a few hundred μW, a qualitatively similar RF spectrum (Fig. S3(c)) is observed - here the mechanical modes are completely dominated by the thermal/free-carrier effects.

Quantitative modeling of this behavior can be accomplished in a manner similar to that of Ref. 7, where the equations of bare optomechanics (evolution of the intracavity optical field amplitude and mechanical position) were augmented by an equation for the cavity temperature increase. We now have to add a fourth differential equation, to account for the change in free carrier population. Following the treatment of thermal and free-carrier terms presented in Ref. 6, we have:

$$
\begin{aligned}
\frac{da}{dt} &= -\frac{1}{2}\left(\Gamma + \alpha_{\mathrm{TPA}}|a(t)|^2 + \beta_{\mathrm{FCA}}N(t)\right)a(t) \\
&\quad + i\left(\delta\omega_c + g_{\mathrm{OM}}x + g_{th}\Delta T(t) + g_{fc}N(t)\right)a(t) + \kappa s \\
\frac{dx}{dt} &= -\Gamma_M\frac{dx}{dt} - \Omega_M^2 x - \frac{|a(t)|^2 g_{\mathrm{OM}}}{\omega_c m} \\
\frac{d\Delta T}{dt} &= -\gamma_{\mathrm{th}}\Delta T(t) + c_{th}\left(\Gamma_{abs} + \alpha_{\mathrm{TPA}}|a(t)|^2 + \beta_{\mathrm{FCA}}N(t)\right)|a(t)|^2 \\
\frac{dN}{dt} &= -\gamma_{\mathrm{fc}}N(t) + \chi_{\mathrm{FCA}}|a(t)|^4
\end{aligned}
$$

where for simplicity we have assumed a single-mode cavity - a more detailed treatment would include both modes of the microdisk and their coupling via backscattering. The first equation describes the intracavity field amplitude $a(t)$, where the first term on the right is its decay due to intrinsic and waveguide loss Γ, two-photon absorption (α_{TPA}) and free-carrier absorption (β_{FCA}), while the second term includes the laser-cavity detuning $\delta\omega_c$ and dispersion due to optomechanical coupling (g_{OM}),

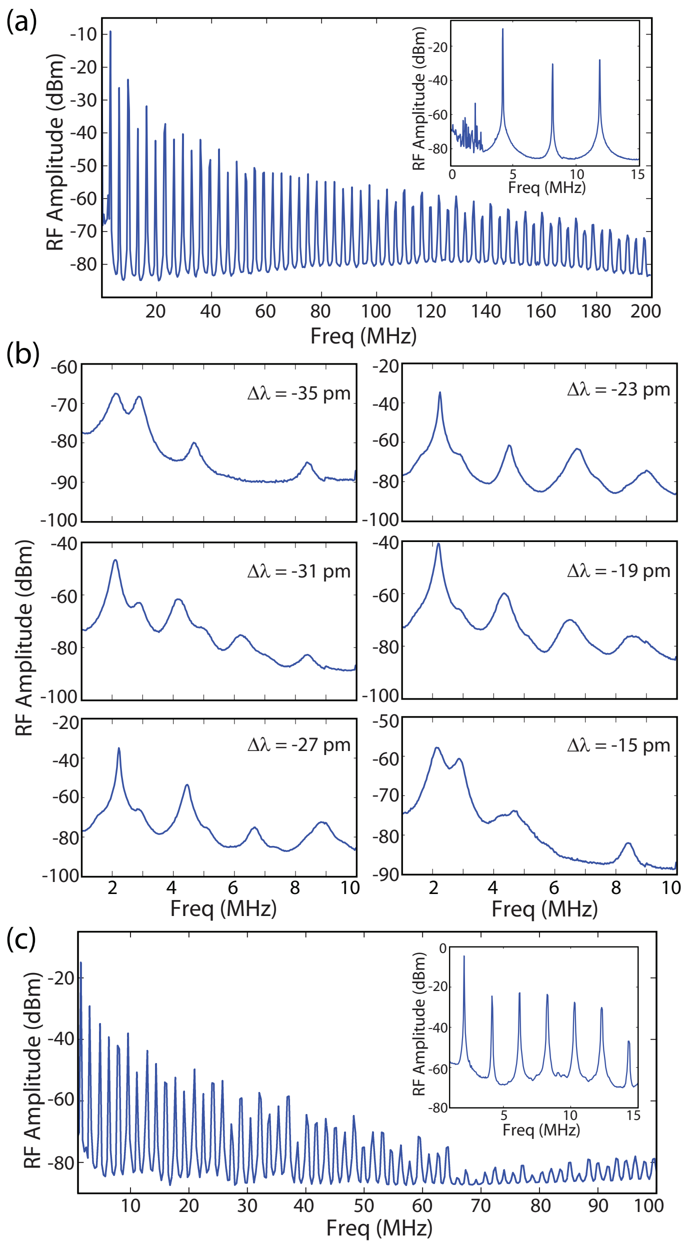

FIG. S3: (a) Broad and zoomed-in RF spectrum of a bare microdisk (no cantilever) with $P_{\text{in}} = 440$ μW coupled to a $Q \approx 3\times10^5$ cavity mode. (b) RF spectra from the cantilever-microdisk system of Fig. S1 as a function of laser-cavity detuning $\Delta\lambda$ with $P_{\text{in}} = 60$ μW coupled to a $Q \approx 1.3\times10^5$ cavity mode. (c) RF spectrum of the cantilever-microdisk system with $P_{\text{in}} \approx 1400$ μW. Inset is a zoomed in high-resolution scan of a portion of the spectrum.

thermo-optic tuning (g_{th}), and free-carrier dispersion (g_{fc}). The second equation describes the mechanical motion $x(t)$ with frequency Ω_M and damping Γ_M and driven by the coupling to the optical field. The third equation describes the cavity temperature change $\Delta T(t)$, where the cavity has a heat capacity c_{th}, the temperature decays with a rate γ_{th}, and is generated by linear absorption (Γ_{abs} is the portion of total optical loss that contributes), two-photon absorption (α_{TPA}), and free-carrier absorption (β_{FCA}). Finally, the fourth equation describes the modal free carrier population $N(t)$, which decays at a rate γ_{fc}' and is generated in proportion to the square of intracavity energy, with proportionality χ_{FCA}. The various coefficients in the above equations are described in detail in Ref. 6, and are a combination of physical properties such as the two-photon absorption coefficient of silicon and the absorption cross-section for free carriers, as well as cavity mode properties such as its group index and different confinement factors and modal volumes weighted according to the electric-field dependence of the given process (e.g., two-photon absorption or free-carrier absorption).

An analysis of the above equations will produce correction terms to the mechanical frequency Ω_M and linewidth Γ_M, and may help provide a better understanding of the power-dependent RF spectra shown in the main text (Fig. 3). For example, Eichenfield *et.al*[7] determined that in their SiN_x photonic crystal nanobeam devices, heating significantly affected the linewidth as a function of detuning, but not the mechanical frequency. In comparison, in addition to linewidth modification (observation of damping for blue-detuned excitation), the frequency dependence on detuning for our devices (Fig. 3(c)-(d) of the main text) does appear to show some effect, in that the shape of the curves near zero-detuning is not nearly as sharply-sloped as the equations of bare optomechanics predict.

H. References

1. S. D. Senturia, *Microsystem Design* (Springer Science+Business Media, New York, NY, 2004), 7th ed.
2. M. Borselli, T. J. Johnson, and O. Painter, Opt. Express **13**, 1515 (2005).
3. A. Schliesser, G. Anetsberger, R. Rivière, O. Arcizet, and T. J. Kippenberg, New Journal of Physics **10**, 095015 (2008).
4. M. Eichenfield, J. Chan, R. M. Camacho, K. J. Vahala, and O. Painter, Nature **462**, 78 (2009).
5. Q. Lin, O. J. Painter, and G. P. Agrawal, Opt. Express **15**, 16604 (2007).
6. T. J. Johnson, M. Borselli, and O. Painter, Opt. Express **14**, 817 (2006).
7. M. Eichenfield, R. Camacho, J. Chan, K. J. Vahala, and O. Painter, Nature **459**, 550 (2009).